Research Article Vol. 16, No. 5 / 1 May 2025 / Biomedical Optics Express 2061
Biomedical Optics EXPRESS

Automated cell properties toolbox from 3D bioprinted hydrogel scaffolds via deep learning and optical coherence tomography

MAHDI BABAEI,[1,†] AARON SHAMOUIL,[1,†] JIAYING WANG,[1] DEEPAK KHARE,[1] TIANYUANYE WANG,[1] MEIJIE SHIH,[1] XIAOJUN YU,[1,2] AND YU GAN[1,3]

[1]Department of Biomedical Engineering, Stevens Institute of Technology, Hoboken, NJ 07030, USA
[2]xyu@stevens.edu
[3]ygan5@steven.edu
[†]These authors contributed equally to this work.

Abstract: Accurately assessing cell viability and morphological properties within 3D bioprinted hydrogel scaffolds is essential for tissue engineering but remains challenging due to the limitations of existing invasive and threshold-based methods. We present a computational toolbox that automates cell viability analysis and quantifies key properties such as elongation, flatness, and surface roughness. This framework integrates optical coherence tomography (OCT) with deep learning-based segmentation, achieving a mean segmentation precision of 88.96%. By leveraging OCT's high-resolution imaging with deep learning-based segmentation, our novel approach enables non-invasive, quantitative analysis, which can advance rapid monitoring of 3D cell cultures for regenerative medicine and biomaterial research.

1. Introduction

In biomaterial engineering, 3D bioprinting has become an innovative method to fabricate complex tissue structures that aid in regenerative processes for both bone and wound healing. [1–3]. The scaffold, within which cells are cultured, creates an environment that closely replicates the natural extracellular matrix and optimizes cell growth capabilities [4]. Engineered scaffolds developed through this approach hold significant potential for a wide range of applications, including regenerative medicine, drug testing, and disease modeling [5,6]. Specifically, hydrogel-based scaffolds have gained prominence in bioprinting for their capability to encapsulate cells and offer tunable mechanical properties that can be modified to represent various tissue structures [7,8]. To evaluate the effectiveness of hydrogel scaffolds, factors such as cell viability and distribution are important to analyze due to their role in facilitating cell proliferation and maintaining structural integrity of the sample [9]. Particularly, high cell viability is essential for cell growth and the long-term functionality of the engineered scaffold, which is vital for clinical applications [10].

Traditionally, techniques to assess cell viability in 3D bioprinted scaffolds, such as histological staining, are invasive and can alter the structure of the sample. Histological methods often require physical manipulation of samples to perform cross-sectional imaging, which limits the capability to perform longitudinal studies on cell growth [11]. Another technique involves fluorescence microscopy that labels cells with fluorescent markers, which can potentially introduce cytotoxicity and photobleaching within delicate hydrogel-based scaffolds [12,13]. These drawbacks make it challenging to collect accurate and repeated measurements over time [14]. In contrast, Optical Coherence Tomography (OCT) offers a non-invasive, label-free alternative that can perform high-resolution imaging of cells within tissue models [15]. OCT has the capability of penetrating deep within 3D gel-based scaffold models with micrometer-level resolution, enabling detailed visualization of cellular structures and scaffold architecture [16]. This makes OCT particularly

#550401 https://doi.org/10.1364/BOE.550401
Journal © 2025 Received 27 Nov 2024; revised 6 Mar 2025; accepted 12 Mar 2025; published 28 Apr 2025

Biomedical Optics EXPRESS

advantageous in the context of evaluating 3D bioprinted hydrogel scaffolds, as it preserves the integrity of the samples while offering comprehensive insights into cell viability and distribution [17,18].

Despite the advantages related to OCT imaging, there remain challenges associated with the time-intensive process of performing manual or threshold-based cell segmentation, which limits the ability to conduct rapid analysis [18,19]. Currently, to the best of our knowledge, there are no existing tools that offer automated analysis of individual cell properties within a 3D environment. Developing such a tool would provide valuable insights into cellular behavior, which is important for monitoring cellular morphology and spatial distribution over time in longitudinal studies [20]. To overcome these challenges, we present a computational toolbox enhanced through deep learning to automate the segmentation of human fetal osteoblast (hFOB) cells within 3D bioprinted hydrogel scaffolds. Additionally, the toolbox provides morphological feature extraction for individual cells within a specified region of interest (ROI), thereby enhancing quantitative evaluation of key cell properties.

For the deep learning-based framework, a U-Net architecture [21] was optimized utilizing VGG-16 [22] as the encoder and integrated with cellular analysis tools to enable 3D evaluation of the bioprinted scaffolds. U-Net, a convolutional neural network (CNN) designed for biomedical image segmentation, incorporates a symmetrical architecture that includes a contracting path for gathering contextual information and an expanding path for precise localization. This design is well-suited for tasks requiring accurate identification and separation of various regions within an image [23]. To enhance feature extraction, a VGG-16 network was integrated within the U-Net model to improve the model's accuracy and capture cellular details within OCT images. Although the implementation of a U-Net and VGG-16 deep learning model has been explored for other segmentation tasks, such as retinal OCT segmentation, these applications primarily focused on layer-wise segmentation of structured retinal features [24]. In contrast, our model is designed to analyze spherical shaped cells within 3D bioprinted hydrogel scaffolds by performing adaptive feature extraction to differentiate individual cells from the surrounding hydrogel. Furthermore, the combination of U-Net and VGG-16 demonstrated significant performance enhancements, providing a robust framework for automated cell segmentation in 3D bioprinted hydrogel scaffolds. This automated approach provides potential for real-time monitoring of cell behavior.

Our automated quantitative toolbox evaluates cell properties such as elongation, flatness, and surface roughness, which provides a more detailed understanding of cell behavior and interactions with the hydrogel scaffold. These metrics are valuable for examining cell behavior as they provide insights for cell-environment interactions, which can influence scaffold function and development. For example, cell elongation is an important indicator of how cells orient themselves within the scaffold, which can affect scaffold organization and the mechanical properties of the bioprinted sample [25]. Cell flatness can indicate how well the cells are adhering to the scaffold surface, which is vital for scaffold integrity and function [25]. Lastly, surface roughness reflects the microenvironment that the cells experience, with implications for cell attachment, proliferation, and differentiation [26]. By quantifying these cell metrics, our study provides a holistic approach to evaluate the morphological properties of cells, which can be leveraged to optimize the design of 3D bioprinted scaffolds within clinical applications. This work represents a significant advancement in tissue engineering, by offering a promising pathway to enhance the quality of engineered scaffolds and accelerate their development for medical applications [27,28].

2. Methods

2.1. Preparation of 3D bioprinted hydrogel scaffolds

In this paper, 3D bioprinting was utilized to fabricate hydrogel scaffolds that contained either alive or dead hFOB cells. These cells facilitated the formation of an isolated environment within a hydrogel matrix, which provides consistency and homogeneity within in vitro models

Biomedical Optics EXPRESS

for cytocompatibility studies [29]. The scaffold design was created using 3D CAD modeling software (SolidWorks) and exported as stereolithography (STL) files for bioprinting. Hydrogel scaffolds were printed using an Allevi 2 bioprinter (3D systems), shown in Fig. 1(a) and had dimensions of 10 mm x 10 mm with a 5 mm infill distance, which is shown in Fig. 1(b).

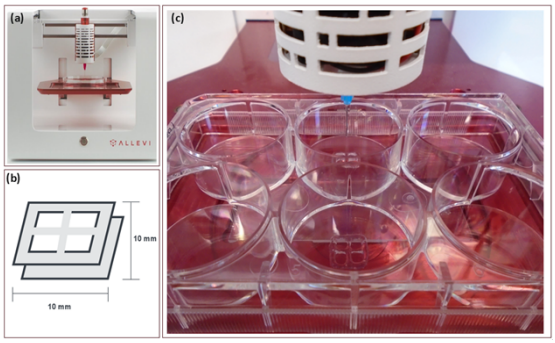

Fig. 1. Demonstration of 3D bioprinting setup. (a) Allevi 2 bioprinter (3D systems). (b) Illustration of the two-layer hydrogel structure for the 3D bioprinted hydrogel scaffold (c) 3D bioprinting of hydrogel scaffold samples.

The hFOB cells were cultured in Dulbecco's Modified Eagle Medium (DMEM), supplemented with 1% penicillin and streptomycin, and 10% fetal bovine serum (FBS). The cells were incubated in 5% CO2 at 37 °C and 95% relative humidity, for one week in cell culture flask. The culture medium was replaced every two days to maintain optimal growth conditions. After reaching confluency of 80-90%, the cells were trypsinized to detach the cells from the flask and centrifuged to obtain the cell pellet. Thereafter, the cell pellet was dissolved using fresh media and then the cells were counted using hemocytometry and optical microscopy.

For bioink preparation, agarose-based hydrogel, a natural polymer extracted from red algae, was considered for 3D printing due to its sufficient stability (without the need of crosslinker), low gelling temperature, and biocompatibility [30,31]. Agarose (2.5 w/v. %) was mixed in phosphate buffer saline (PBS) followed by heating and stirring. The heating and stirring process was complete once a transparent and homogeneous solution was achieved. Afterwards, the alive cells were gently mixed with the agarose solution (20,000 cells per layer). In parallel, the same quantity of cells underwent heat treatment (80°C) for 10 minutes to obtain dead cells and were gently mixed with the agarose solution. Two distinct bioinks were prepared: one containing alive cells suspended in agarose and the other containing dead cells mixed with agarose, enabling the bioprinting of separate scaffolds for alive and dead cell samples.

For bioprinting, the bioink was calibrated and chilled at -20°C to achieve optimal printing conditions. Afterwards, the bioink was loaded into a bioprinter, which was programmed to deposit the bioink layer by layer onto a petri dish, creating a 3D structure with precisely distributed cells embedded within the hydrogel scaffold, as shown in Fig. 1(c). This bioprinting technique not only allowed for the precise placement of cells within the 3D structure but also facilitated the creation of a controlled environment for studying the behavior of both alive and dead cells within the engineered scaffold. The resulting 3D scaffolds were utilized for the subsequent analysis of cell viability, distribution, and interaction within the hydrogel matrix.

2.2. Optical coherence tomography (OCT) imaging

For the imaging process, data was acquired from a benchtop spectral domain (SD) OCT [32] system (Thorlabs Ganymeade) following our previous studies [33,34]. Regarding optical resolution [35], the system has an axial resolution of 3 μm and a lateral resolution of 4 μm,

Biomedical Optics EXPRESS

both in air. Moreover, the system has digital resolutions of 2.00 µm on both axial and lateral direction. Noticeably, optical resolution defines the system's capability to resolve two point-sources with equal intensity. In contrast, digital resolution [36], is defined by the distance per pixel in each image. The imaging acquisition process is illustrated in Fig. 2(a-b). OCT acquires B-scans by capturing cross-sectional images of the hydrogel scaffolds through the acquisition of depth-resolved reflectivity profiles along a specified lateral axis. The imaging process involved transporting samples from a 6-well culture plate to a culture dish, ensuring stable conditions for OCT imaging. These B-scans are essentially 2D slices that represent the internal structure of the scaffold, allowing for detailed visualization of cell distribution and morphology. In this paper, we acquired two types of 3D images: 2D B-scan over time (MB-scanning) and 3D volumes.

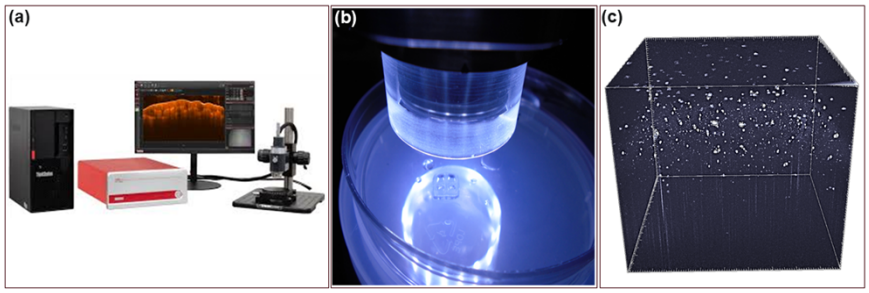

Fig. 2. OCT image acquisition. (a) Thorlabs OCT system. (b) Placement of the 3D bioprinted hydrogel scaffold sample when performing OCT imaging. (c) OCT volume for representative scaffold sample.

To achieve rapid monitoring of the hydrogel scaffolds, MB-scanning was utilized to perform sequential B-scan acquisitions at a fixed lateral position, enabling time-series analysis of cell viability and optical intensity fluctuations. MB-scanning, as described in prior studies by Yasuno and Tearney's research groups [37,38], allows for dynamic monitoring of cellular activity and structural properties within biological tissues. This method has been widely utilized in dynamic OCT imaging and provides valuable insights for time-dependent cell behavior [20]. Each B-scan acquired during MB-scanning consisted of 1,024 × 1,024 pixels. The OCT system operated at an A-scan rate of 100 kHz, meaning that 100,000 A-scans were acquired per second. For the time-series dataset, each B-scan was recorded every 5 seconds over a 3- minute period, resulting in 36 sequential frames for each region of the corresponding scaffold sample. To ensure the integrity and viability of the cells during imaging, each sample was placed in a cell culture medium that closely mimics the natural extracellular environment. This setup helped maintain cell health and activity throughout the imaging process.

For 3D volumetric acquisition, illustrated in Fig. 2(c), each volume was 1,024 × 1,024 × 1000 pixels, covering a spatial volume of 2 mm x 2 mm x 1.99 mm. This allowed for a detailed reconstruction of the scaffold's 3D structure, providing insights into the spatial arrangement and distribution of cells within the hydrogel matrix. The imaging process was carefully timed and managed to minimize cell exposure to external conditions, thereby preserving cell viability and ensuring accurate representation of the scaffold's dynamic behavior throughout the imaging period.

2.3. Deep learning-based segmentation

The methodology's workflow is illustrated in Fig. 3, starting with the pre-processing of OCT images, progressing to deep learning-based segmentation, followed by post-processing and quantitative analysis of cell viability and visualization. The pre-processing phase starts by slicing 3D volumetric OCT images into B-scans, which are cross-sectional representations of

Biomedical Optics EXPRESS

cell structure inside the hydrogel sample. This transformation is crucial for formatting the data in a manner that deep learning algorithms can analyze efficiently. Each B-scan defines a narrow segment of volumetric data, enabling the model to explore cellular spatial features independently. Subsequently, contrast normalization is implemented by histogram equalization, a method that improves image clarity and standardizes intensity fluctuations throughout the dataset [39]. Adjusting the contrast enhances the visibility of cell borders, which facilitates the neural network's detection of essential features during segmentation.

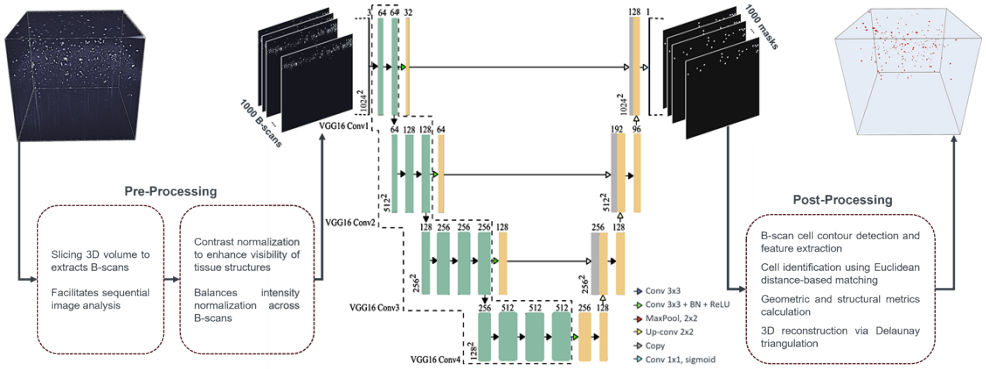

Fig. 3. Illustrates the complete workflow, starting with the preprocessing of OCT images, followed by deep learning-based segmentation, and concluding with detailed post-processing and quantitative analysis to access cell viability and distribution.

The deep learning segmentation model utilized a U-Net architecture enhanced with a VGG-16 encoder that extracts features from each B-scan via a sequence of 3×3 convolutional layers, each succeeded by ReLU activations [40] and Batch Normalization [41] to maintain stable training. Max-pooling layers [42], interspersed among these blocks, progressively diminished the spatial dimensions of the feature maps while increasing their depth, allowing the network to capture more complex representations. At the bottleneck, the encoder compressed the feature maps into their most abstract representation, capturing high-level information essential for differentiating cells from the background. The decoder subsequently reconstructed the spatial dimensions of the feature maps via 2×2 up-convolution layers. Skip connections were integrated between corresponding layers of the encoder and decoder, allowing the network to preserve fine-grained spatial information by combining high-resolution details from the encoder with the abstract features in the decoder. The combination of information was essential for achieving accurate segmentation. The final segmentation map was generated by employing a 1×1 convolution followed by a sigmoid activation function, resulting in a binary classification for each pixel in the image that defines regions of interest, specifically the cells, from the background. During the training process, some of the B-scans were organized into a coherent training dataset. Binary masks were generated to label regions of interest, providing ground truth annotations by pairing each B-scan with its corresponding mask. These paired B-scans and masks were used as training data for the proposed model.

Upon completion of segmentation, a sequence of post-processing steps was implemented to identify cells, ensuring accurate detection throughout the B-scan sequence. The post-processing phase began with cell contour identification, which defined the outer boundaries of each segmented cell, followed by a cell-reconstruction technique that utilized Euclidean distance. This approach computed the Euclidean distance between cells in successive B-scans to locate and connect corresponding cells across frames. If the distance between two cells over consecutive frames were below a specified threshold of N_C pixels, the algorithm denoted them as the same cell.

Biomedical Optics EXPRESS

This distance-based matching accurately monitored cell positions during the B-scan sequence and facilitated the reconstruction of three-dimensional cell structures by connecting segmented regions across layers. The 3D reconstruction provided insights into cell alignment and continuity throughout the entire hydrogel scaffold volume. Quantitative analysis was then conducted on the reconstructed 3D model to evaluate cell viability and spatial distribution, which were essential for understanding the biological properties of the hydrogel scaffolds.

2.4. Quantitative evaluation of metrics

A comprehensive evaluation of the segmentation model and the morphological properties of reconstructed cells is essential to ensure both the accuracy of the segmentation process and the biological relevance of the extracted cell metrics. In this study, two categories of quantitative metrics were analyzed: those assessing the performance of the segmentation model and those characterizing the structural attributes of individual cells.

2.4.1. Segmentation evaluation metrics

To evaluate the segmentation performance of the model, both precision and accuracy were computed. Precision is a key metric that quantifies how well the model identifies cells while minimizing false detections. It measures the proportion of correctly identified cell pixels among all pixels classified as cells by the model, ensuring that misclassified background pixels do not artificially inflate performance. Precision is defined as

$$Precision = \frac{True\ Positives\ (TP)}{True\ Positives\ (TP) + False\ Positives\ (FP)} \tag{1}$$

where true positives represent correctly identified cell pixels, and false positives correspond to background pixels mistakenly classified as part of a cell. A high precision score indicates that most of the detected cell pixels are indeed part of real cells, reducing false positives that could lead to inaccurate morphological analysis.

While accuracy is a widely used metric in segmentation tasks, it is less informative in this study due to the significant imbalance between cell and background pixels. Accuracy is calculated as

$$Accuracy = \frac{True\ Positives\ (TP) + True\ Negatives\ (TN)}{Total\ Pixels} \tag{2}$$

where true negatives represent correctly identified background pixels. In this study, if background region takes a large portion of the image (usually 94% to 98% of pixels), in which the number of true negative pixels are much larger than the number of true positive pixels. An improvement in obtaining true positive pixels reflects a minor change in accuracy. It is possible that a model that classifies most pixels as background will achieve high accuracy, even if it fails to properly segment cells. This can lead to an overestimation of model performance, as a high accuracy score may primarily reflect the correct identification of background rather than the correct detection of cellular structures. Given this limitation, precision serves as a more reliable metric for evaluating segmentation quality, as it directly measures how effectively the model distinguishes cells from the background.

2.4.2. Cell properties evaluation metrics

In this study, we developed a set of functions for quantitative evaluation of several morphological metrics to analyze the structural qualities of cells within the reconstructed 3D hydrogel scaffold volume. The 3D reconstruction of each cell allows for the calculation of specific morphological properties such as elongation, flatness, and surface roughness, which provides insights into the morphological properties of each cell. Principal component analysis (PCA) [43] was used to

Biomedical Optics EXPRESS

determine the shape of each cell by analyzing the spatial distribution of its points along the principal axes of variation. Additionally, PCA was used to extract orthogonal principal axes that describe the cell's major structural orientation, which allows for quantitative representation of cell morphology. The radii along the principal axes were computed as the difference between the maximum and minimum extents of the transformed points in PCA space. This provides a geometric basis for assessing how cells interact with the hydrogel scaffold by distinguishing any abnormalities for cell shape.

Elongation was calculated to assess the degree to which each cell was stretched along its principal axis. As shown in Eq. (3), the elongation metric represents the ratio of the largest radius ($R_{\{largest\}}$) to the intermediate radius ($R_{\{medium\}}$) of the cell [25]. A higher elongation value indicates a more elongated cell shape, which is often associated with cellular differentiation or structural adaptations within the hydrogel matrix.

$$Elongation = R_{\{largest\}}/R_{\{medium\}} \tag{3}$$

Flatness was measured as the ratio between the intermediate and smallest axes, as defined in Eq. (4) [25]. This metric describes how compressed or flattened a cell is, offering insights into its structural properties. Cells with high flatness values tend to have an irregular shape, which may reflect certain biological behaviors or external pressures exerted within the scaffold environment. By comparing the intermediate ($R_{\{medium\}}$) and smallest radii ($R_{\{smallest\}}$), we captured variations in cellular morphology indicative of structural flattening.

$$Flatness = R_{\{medium\}}/R_{\{smallest\}} \tag{4}$$

Surface roughness was calculated to quantify the texture of each cell's surface. This metric, as shown in Eq. (5), compares the cell's surface area to its volume, providing a measure of surface irregularity [26]. Cells with higher surface roughness values exhibit a more complex, textured surface, which may be indicative of cellular processes such as surface modifications or adhesion dynamics.

$$Surface\ Roughness \equiv (Surface\ Area/4\pi)^{1/2}/(3{*}Volume/4\pi)^{1/3} \tag{5}$$

Upon completing the morphological analysis, properties from each cell were systematically recorded. These metrics were compiled into a dataset, creating a comprehensive profile of cell properties within the reconstructed 3D scaffold volume. This data provided a comprehensive profile of cell metrics within the reconstructed 3D scaffold volume, allowing for detailed investigations into cell morphology.

3. Results

3.1. Segmentation model results

The model was trained using a dataset of 600 imaging pairs, where each pair consisted of a 2D OCT image and a corresponding binary mask that identified cell locations within a specific B-scan. The value of N_C was set to be 10, according to the regular size of cells. Binary masks were manually created to serve as ground truth for training. The model was trained on an RTX A6000 GPU.

A 5-fold cross-validation was performed to evaluate the generalizability of the model. For each fold, the dataset was split by sample, where each fold contained two 3D bioprinted hydrogel scaffold images acquired on the same day. This approach ensured that the model was exposed to a variety of data and helped mitigate the risk of overfitting to specific samples. During training, the images were preprocessed by normalizing the pixel values and data augmentation techniques such as image flipping and intensity noise, were applied to introduce variability in training samples. Each fold consisted of a complete training cycle, where the model was trained for 100 epochs

Biomedical Optics EXPRESS

with a batch size of 2. After each training cycle, the model's performance was evaluated on the test set of the respective fold. The segmentation stages of the model are visually demonstrated in Fig. 4.

Fig. 4. Comparison of cell segmentation stages. (a): Raw OCT image showing the cell distribution within the sample. (b): Binary mask highlighting segmented cells, isolating cellular structures from the background. (c): Segmentation result. Scale bars represent 250 micrometers.

To evaluate the segmentation model's performance, we report precision as the primary metric because it directly measures how well the model identifies cells while minimizing false detections. A high precision means that most of the detected cells are indeed real cells, reducing false positives, which is crucial for biological analysis. On the other hand, accuracy is a widely used metric but is not suitable for this study due to the overwhelming presence of background pixels in the images. Since the background occupies the majority of the image, even a model that misses many cells but correctly classifies the background can still achieve a high accuracy. This makes accuracy misleading, as it does not reflect how well the model segments actual cells. The precision scores for each fold were recorded to assess the variability of the model's performance across different subsets of the data.

Precision values for each fold ranged from 78.6% to 92.1%, with a mean precision of 88.96% across all folds. Accuracy value for each fold ranged from 98.1% to 99.7%, with a mean accuracy of 99.1% across all folds. As mentioned in Section 2.4, the value of accuracy is much higher than the value of precision as large portion of image belongs to background. Additionally, the cell detection rate was calculated based on the overlap between predicted cell regions and ground-truth annotations. The model achieved an average cell detection rate of 85.90% across all folds, demonstrating its ability to successfully identify the majority of cells present in the dataset. These results indicate consistent model performance, with the model effectively identifying cells within the OCT images in each test set. A summary of the model's performance metrics is presented in Table 1.

Table 1. Average segmentation performance across all folds, reporting mean precision and mean cell detection rate.

Metric	Value (%)
Mean Precision at Pixel Level	88.96
Detection Rate at Cellular Level	85.90

3.2. Cell viability

The viability of cells was assessed by measuring the intensity levels of alive and dead cells through M-scanning of 2D OCT images over a 3-minute period. Figure 5 illustrates the intensity changes in regions of interest (ROIs) associated with both alive and dead cells, where the mean intensity is calculated from all pixels within each segmented cell region. This ensures that the intensity measurements reflect the optical properties of the entire cell rather than individual pixel variations.

From the intensity-time plot, the intensity levels between the alive and dead cells exhibit significant differences, which can be attributed to their corresponding cellular behavior. The alive

Biomedical Optics EXPRESS

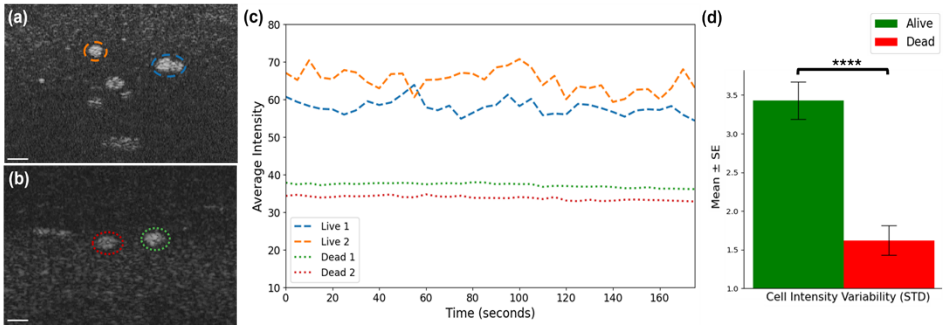

Fig. 5. (a) 2D OCT image showing representative alive cells. (b) 2D OCT image showing representative dead cells. (c) Graph illustrating the average light intensity over time for two alive and two dead cells, with measurements taken every 5 seconds over a total duration of 180 seconds. (d) Statistical comparison of intensity variability (standard deviation) between alive and dead cells. For each cell, the standard deviation of intensity fluctuations was calculated over the 180-second period based on measurements taken every 5 seconds. The mean standard deviation for each group was then obtained by averaging the individual cell standard deviations across more than 50 alive and 50 dead cells. A two-sample t-test confirmed a statistically significant difference, demonstrating that alive cells exhibit greater temporal intensity variations compared to dead cells. . *: $p < 0.5$; **: $p < 0.01$; ***: $p < 0.001$; ****: $p < 0.0001$. Scale bars represent 20 micrometers.

cells show relatively higher intensity values, fluctuating in the range of 55–70 mean intensity units throughout the observation period. This variation reflects the dynamic nature of living cells, which maintain active cellular processes [44]. Additionally, the fluctuations in the intensity levels of alive cell ROIs are likely due to physiological changes in cellular morphology and activity during the observation period. In contrast, the intensity values remained relatively stable for dead cells, showing only minimal fluctuations. The intensity levels for dead cells were notably lower, remaining in the range of 30–40 mean intensity units. The lower intensity levels for dead cells reflected a lack of metabolic or structural activity, consistent with the loss of cellular integrity typically seen in non-viable cells [44]. Furthermore, the stability of intensity in dead cells suggested that there are no significant changes in their optical properties over time, further confirming their non-viable status.

To quantitatively assess temporal intensity variations between groups, the standard deviation (std) of intensity fluctuations was first calculated for each cell over the 180-second period, with measurements taken every 5 seconds. The mean std was then computed across 50 alive and 50 dead cells to obtain a representative measure for each group. Statistical validation using a t-test (Fig. 5(d)) confirmed that alive cells exhibited significantly greater intensity variability compared to dead cells, reinforcing the robustness of intensity fluctuations as a reliable metric for distinguishing viable from non-viable cells.

3.3. MB-scan time-series analysis and cell monitoring

We applied our segmentation methodology on MB-scan OCT images, enabling the segmentation and analysis of cell distributions over sequential frames within the time-series data. For each B-scan, the trained segmentation model produced a binary mask. Contours of the segmented regions were identified, and their centroids were calculated using image moments to determine the cell's central coordinates, with the previously described Euclidean distance-based method used to connect corresponding cells across frames. Figure 6 illustrates our analysis for the positioning of individual cells at three distinct time intervals: T = 0s, T = 90s, and T = 180s. The

Biomedical Optics EXPRESS

segmented cells were monitored to analyze their movement and shape alterations. This approach provides potential to monitor interactions between multiple cells over longer periods of time, which can provide further insight regarding cell tracking and proliferation within a bioprinted hydrogel scaffold.

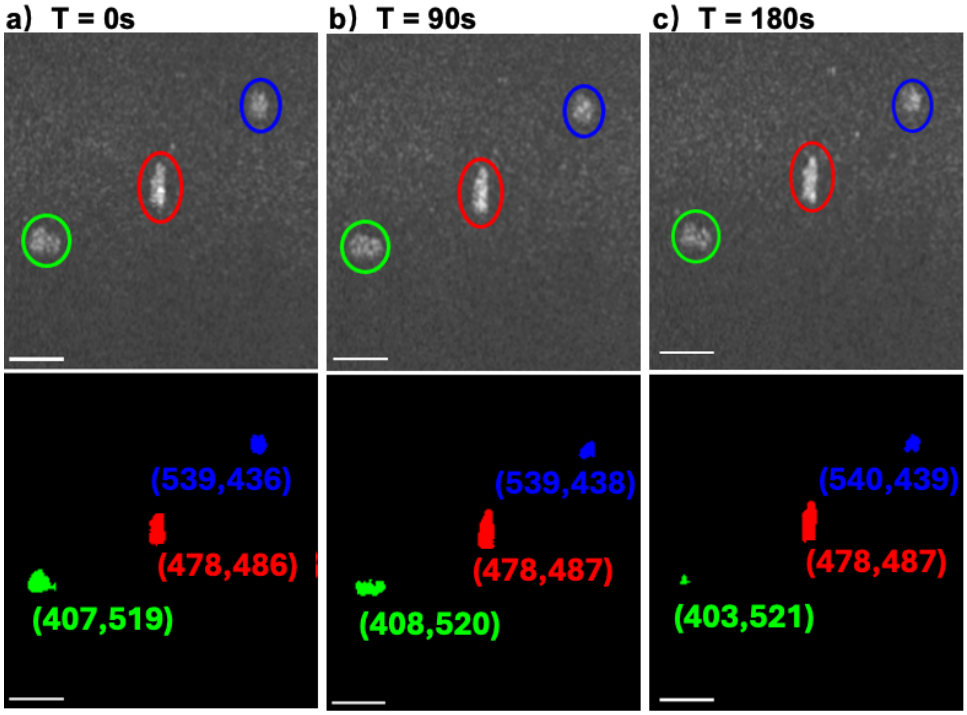

Fig. 6. Time-Series Analysis of Cell Movement in M-Scan OCT Images. Cells were segmented and tracked across three different time points: T = 0s (a), T = 90s (b), and T = 180s (c). The colored regions represent individual cells, with their positions annotated. Scale bars represent 20 micrometers.

3.4. 3D cell reconstruction and cell properties

The process began with the extraction of individual B-scans from the 3D OCT volume. Once each B-scan was extracted, the trained segmentation model predicted a binary segmentation mask. Using the predicted binary mask, contours of the segmented regions were identified and extracted. For each detected contour, the centroid was calculated using image moments, which provided a statistical representation of the contour's shape and allowed for the derivation of the cell's central coordinates. To ensure the quality and relevance of the identified cells, segmented regions appearing in fewer than three frames were excluded from further analysis, as they are likely to represent noise or artifacts.

After identifying relevant cells and extracting their contours from each frame, 3D reconstruction of the cells was performed. Using the points derived from the identified contours, Delaunay triangulation was applied to construct a 3D mesh for each cell, enabling a detailed visualization of cellular structure in three dimensions. To efficiently manage, analyze, and process these meshes, we utilized trimesh, a Python library specifically designed for handling and manipulating triangular mesh structures [45]. Trimesh operates by representing 3D objects as a set of connected triangular faces, allowing for efficient computation of surface area, volume, and curvature. The library provides built-in tools for mesh smoothing, resampling, repairing, and feature extraction,

Biomedical Optics EXPRESS

making it particularly useful for biomedical imaging applications. Moreover, trimesh allows for geometric transformations, convex hull estimation, and Boolean operations (e.g., union, difference, and intersection of meshes), which are critical for refining and validating segmented structures [46].

Once the 3D meshes were generated, various geometric and structural metrics were computed. Surface area was calculated directly from the sum of the areas of all triangular faces in the mesh. Surface roughness was determined by analyzing the variance in local curvature and the number of frames in which the cell appeared, reflecting fluctuations in cell shape over time. Additionally, principal component analysis (PCA) was applied to the set of 3D points defining each cell's geometry, allowing for precise calculations of cell elongation and flatness. The integration of trimesh streamlined these calculations by providing optimized mesh processing functions and numerical robustness, ensuring an accurate characterization of cellular structures.

The 3D visualizations, shown in Fig. 7, illustrate both cell distribution across the sample and the detailed structure of individual cells. The left plot shows the spatial arrangement of cells, while the enlarged view on the right provides a direct comparison between a cell segmented by the model and its manually annotated counterpart. As discussed in Section 2.4, precision was selected as the primary metric for assessing segmentation performance due to its ability to directly measure how well the model identifies cells while minimizing false detections. The segmentation model achieved a precision score of 91.02%, demonstrating strong agreement with manual annotations. Although overall accuracy was computed and found to be 99.72%, this metric is less informative in this context due to the dominance of background pixels in the images.

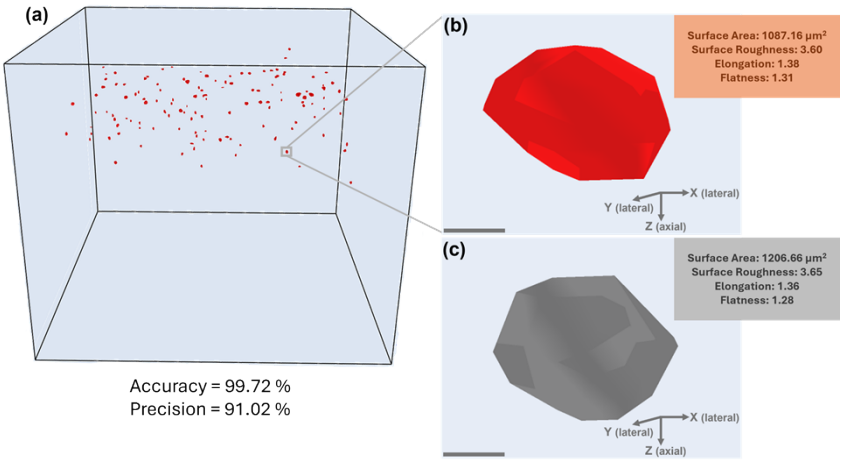

Fig. 7. 3D visualization of an individual cell from the generated environment and corresponding measured properties. (a) Spatial distribution of segmented cells within the hydrogel scaffold. (b) 3D reconstruction of a cell segmented by the model, with extracted morphological metrics. (c) Manually annotated counterpart of the same cell for comparison. The displayed metrics are used for comparing the two cells. Scale bars represent 5 micrometers.

To perform further analysis of the 3D imaging volumes, there were calculations performed to determine the elongation, flatness, and surface roughness of both alive and dead cells. For visualization of these properties, a pre-defined 3D dynamic window was created to identify the corresponding metrics of each cell. For comparison, eight different hydrogel scaffold samples were examined for both alive and dead cells. Furthermore, to account for the relative diameter of alive cells we considered a range from 20 µm - 30 µm, based on previous research studies that reported an average of 25 µm for hFOB cells [47]. For the dead cell samples, we considered the

Biomedical Optics EXPRESS

cell shrinkage that typically occurs for cells that are placed in high temperature conditions [48]. Since previous research was not available regarding the diameter of dead hFOB cells, we analyzed the cell shrinkage percentage related to other cell types and considered a percentage diameter decrease of 20% for the lower range and 30% for the upper range relative to the alive cells [49,50]. To assess statistical significance in mean differences of elongation, flatness, and surface roughness between alive and dead cells, a t-test was performed at a 95% confidence interval. After further calculations, shown in Fig. 8, we observed statistically significant differences associated with alive cells having greater surface elongation and flatness compared to dead cells, while surface roughness was greater for dead cells compared to alive cells. This comprehensive analysis provided a detailed characterization of the cells within the 3D bioprinted scaffold, offering valuable insights into cellular behavior and interaction with the scaffold.

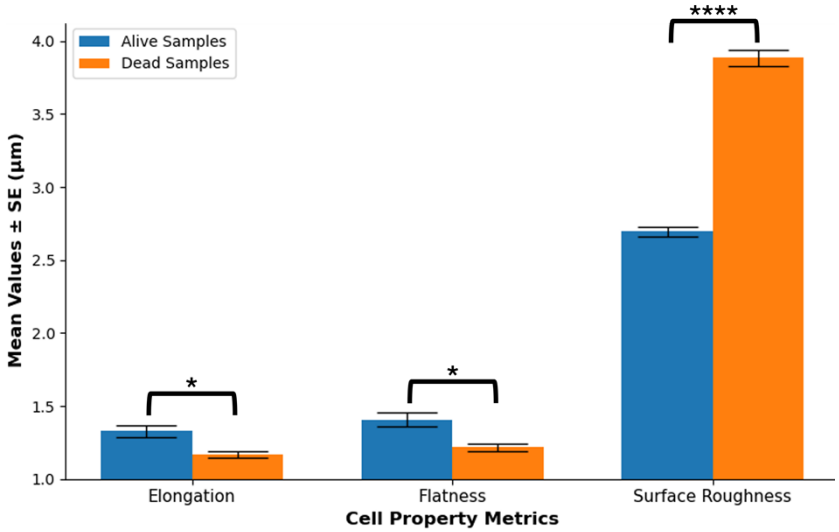

Fig. 8. Graphical comparison for the average cell property metrics (elongation, flatness, and surface roughness) for both alive and dead cells within corresponding 3D bioprinted scaffolds. *: $p < 0.5$; **: $p < 0.01$; ***: $p < 0.001$; ****: $p < 0.0001$

4. Discussion

4.1. Significance of automated toolbox

The development of an automated computational toolbox provides an end-to-end solution for analyzing cell viability and distribution within 3D bioprinted hydrogel scaffolds. A key feature of this toolbox is the user-defined region of interest (ROI) selection, which allows for the examination of both overall cell distribution and individual cell metrics within specified regions of the reconstructed 3D volume. This flexible ROI-based approach offers several advantages. First, it enables targeted analysis of specific scaffold regions, facilitating the assessment of localized cell density, morphology, and interactions. Second, by selecting and analyzing different ROIs, there can be investigations of spatial variations in cell distribution, identifying areas of high or low cell density, and potential patterns of cellular adaptation within the scaffold. Lastly, this visualization method enhances the study of spatial heterogeneity in cell metrics, such as surface roughness, elongation, and flatness, which allows for direct comparisons between different scaffold regions.

Our automated toolbox processes entire volumetric datasets efficiently, with a processing time of 0.3 second for one B- total processing time of 5 minutes per 3D volume, providing a fast

Biomedical Optics EXPRESS

and reproducible analysis pipeline. The input to the toolbox consists of OCT image volumes, while the output includes segmented 3D cell reconstructions and quantitative morphological metrics. A limitation of a prior dynamic OCT (D-OCT) study was the lack of a 3D automated segmentation framework to monitor individual cell activity, morphology, and distribution over time, which restricted their ability to perform longitudinal studies for disease modeling applications [20]. While previous approaches mentioned earlier have demonstrated the ability of D-OCT to recognize cells, they often rely on manual or intensity-based segmentation, making it difficult to achieve reliable monitoring of cellular dynamics. Our automated toolbox addresses this gap by providing 3D segmentation and morphological tracking, allowing for single-cell level analysis across multiple time points. By integrating automated segmentation, ROI selection, and morphological analysis, this toolbox enhances the efficiency and accuracy of cell behavior assessment in bioprinted scaffolds.

4.2. Interpretation of results and implications for tissue engineering

From our results, we identified several key properties of hFOB cells that were cultured within a 3D hydrogel sample, particularly focusing on cell viability and morphological properties. The data indicates that optical coherence tomography (OCT) can be effectively utilized to monitor cell intensity levels over time, offering a non-invasive method for assessing the viability and distribution of cells within the hydrogel scaffold.

In our study, we also developed an automated quantitative toolbox to analyze the 3D OCT volumes, enabling comprehensive cell segmentation and evaluations of cell properties such as elongation, flatness, and surface roughness at the individual cell level. Our findings revealed statistically significant differences, with elongation and flatness being higher in alive cells compared to dead cells. This aligns well with previous research demonstrating that the elongation and flatness of viable hFOB cells tend to increase over time due to enhanced cytoskeletal interactions and cell-cell communication [51]. Additionally, surface roughness calculations revealed a statistically significant difference corresponding to dead cell samples exhibiting higher values compared to alive cell samples. Similarly, our research aligns with previous studies, which show that heat treatment of tissue scaffolds induces morphological changes, causing cells to adopt more complex geometries and deviate from their spherical shape, thereby increasing surface roughness [52,53].

These morphological changes reflect active cellular processes, including proliferation, migration, and differentiation, which are important factors for effective cellular regeneration [54] . The ability to monitor these cell properties rapidly not only enhances our understanding of cell behavior within the engineered scaffold, but also provides valuable insights regarding scaffold function. Assessing the progression of these morphological features can inform us about the health and functional state of the cells and the overall efficacy of certain biomaterials in facilitating bone healing [55]. Such metrics are essential for evaluating the potential of 3D bioprinted scaffolds in clinical applications, where the interaction between cells and the biomaterial significantly influences the effectiveness of tissue engineering methods [54]. Ultimately, our findings highlight the importance of using OCT combined with deep learning to facilitate rapid monitoring of cell dynamics, which can help for future research and development studies in tissue engineering.

The integration of an automated toolbox for evaluating cell viability and morphology in 3D bioprinted scaffolds represents a promising advancement in biomaterial research by providing a precise and non-invasive method to analyze cell behavior within engineered scaffolds. Traditional methods, such as fluorescence staining, often introduce invasive and cytotoxic effects to the scaffold, potentially altering cellular behavior and leading to inaccurate assessments of cell viability [56]. Additionally, these methods were typically applied to simpler systems, such as 2D monolayers or traditional histological sections, where the complexity of the scaffold environment is significantly reduced compared to 3D bioprinted structures [57]. Regarding OCT, prior studies

Biomedical Optics EXPRESS

have demonstrated its effectiveness in imaging hydrogel scaffolds and differentiating scaffold microstructures, porosity, and cell viability [54,58]. However, these approaches primarily relied on manual image analysis and intensity-based segmentation, which limit their applicability to provide rapid cell property assessments. Unlike these previous traditional and OCT-based studies, our work introduces a deep learning-enhanced computational toolbox that automates individual cell segmentation, morphological analysis, and viability assessments within 3D bioprinted hydrogel scaffolds. By integrating MB-scanning within our dataset, there was comprehensive assessment for evaluating dynamic monitoring of cell behavior and optical intensity fluctuations over time. This capability addresses the challenges of rapid cell property analysis and providing quantitative assessment of cell viability within bioprinted scaffolds.

4.3. Limitations and potential improvements

While our study provides valuable insights regarding cell viability and morphology within 3D hydrogel samples, several limitations must be addressed to improve the robustness and generalizability of our findings. The morphological metrics for the automated toolbox, including elongation, flatness, and surface roughness, were derived from 3D volumes captured at a single time point rather than time-lapse imaging. This approach was selected to accommodate the OCT system's acquisition speed limitations, while also preserving cell viability throughout the imaging process. Although real-time analysis was not achieved for this study, advances in GPU acceleration, parallel computing, and neural network distillation offer potential pathways for reducing processing times and acquiring near real-time assessments in future iterations of this framework. For the scope of cell types investigated, our study focused exclusively on hFOB cells within a hydrogel sample, which limits the applicability of these findings to other cell types. Particularly, factors such as cell morphology and differentiation may vary when cells interact with different biomaterials, potentially affecting viability and structural properties in similar 3D environments. Future research should expand to include a variety of cell types and biomaterial interactions to explore these potential variations and strengthen the generalizability of our findings. Addressing these limitations through a broader range of cell studies, improved deep learning algorithms, and increased sample diversity will enhance the reliability and applicability of this methodology for assessing cell viability and biomaterial compatibility for 3D bioprinted scaffolds.

5. Conclusion

We present an automated computational toolbox that integrates OCT and deep learning for hFOB cell segmentation along with quantitative analysis for 3D bioprinted hydrogel scaffolds. This framework allows for the evaluation of cell viability and morphological properties for individual cells within a user selected ROI. Unlike traditional methods, this approach preserves scaffold integrity and establishes a foundation for longitudinal studies to monitor cell behavior over time. Our findings reveal statistically significant differences in elongation, flatness, and surface roughness between live and dead cells, emphasizing the importance of morphological analysis in viability assessments. By leveraging OCT imaging with a U-Net-based segmentation model enhanced by VGG-16, the toolbox enables quantitative evaluation of 3D bioprinted scaffolds. Future investigations could incorporate 3D time-lapse imaging to capture dynamic cellular responses and interactions within biomaterials, further enhancing biomaterial research and scaffold optimization. This framework provides an innovative approach within tissue engineering to evaluate 3D bioprinted scaffolds using deep learning and demonstrates potential to improve the development of bioprinted scaffolds for future clinical applications.

Funding. National Science Foundation (2239810); New Jersey Health Foundation (PC10-23); AI Research in Summer Fellowship Program at Stevens..

Biomedical Optics EXPRESS

Acknowledgements. The authors would like to thank the support from NSF-CAREER (award no. 2239810, YG), New Jersey Health Foundation (award no. PC10-23, XY), and AI Research in Summer Fellowship Program at Stevens (MS).

Disclosures. The authors declare no conflicts of interest

Data Availability. Data underlying the results presented in this paper are not publicly available at this time but may be obtained from the authors upon reasonable request.

References

1. L. Bai, G. Tao, M. Feng, *et al.*, "Hydrogel drug delivery systems for bone regeneration," Pharmaceutics **15**(5), 1334 (2023).
2. X. Ding, Y. Yu, and W. Li, "*In situ* 3D-bioprinting MoS_2 accelerated gelling hydrogel scaffold for promoting chronic diabetic wound healing," Matter **6**(3), 1000–1014 (2023).
3. M. Deptuła, M. Zawrzykraj, and J. Sawicka, "Application of 3D- printed hydrogels in wound healing and regenerative medicine," Biomed. Pharmacother. **167**, 115416 (2023).
4. M. J. Lerman, J. Lembong, and G. Gillen, "3D printing in cell culture systems and medical applications," Appl. Phys. Rev. **5**(4), 041109 (2018).
5. A. Revete, A. Aparicio, B. A. Cisterna, *et al.*, "Advancements in the use of hydrogels for regenerative medicine: properties and biomedical applications," Int. J. Biomater. **2022**, 1–16 (2022).
6. S. Maji and H. Lee, "Engineering hydrogels for the development of three-dimensional in vitro models," Int. J. Mol. Sci. **23**(5), 2662 (2022).
7. X. Li, Q. Sun, Q. Li, *et al.*, "Functional hydrogels with tunable structures and properties for tissue engineering applications," Front. Chem. **6**, 499 (2018).
8. G. Castellano, A. Stasi, A. Intini, *et al.*, "Endothelial dysfunction and renal fibrosis in endotoxemia-induced oliguric kidney injury: possible role of LPS-binding protein," Crit. Care **18**(5), 520 (2014).
9. A. J. Dominijanni, M. Devarasetty, S. D. Forsythe, *et al.*, "Cell viability assays in three-dimensional hydrogels: a comparative study of accuracy," Tissue Eng. Part C Methods **27**(7), 401–410 (2021).
10. C.-C. Hsu, J. H. George, S. Waller, *et al.*, "Increased connectivity of hiPSC-derived neural networks in multiphase granular hydrogel scaffolds," Bioact. Mater. **9**, 358–372 (2022).
11. C. Dunn, D. Brettle, M. Cockroft, *et al.*, "Quantitative assessment of H&E staining for pathology: development and clinical evaluation of a novel system," Diagn. Pathol. **19**(1), 42 (2024).
12. J. Zhong, T. Zhao, and M. Liu, "Fluorescence microscopic visualization of functionalized hydrogels," NPG Asia Mater. **14**(1), 38 (2022).
13. M. Zhang, Z. Wang, P. Huang, *et al.*, "Real-time and noninvasive tracking of injectable hydrogel degradation using functionalized AIE nanoparticles," Nanophotonics **9**(7), 2063–2075 (2020).
14. A. Ettinger and T. Wittmann, "Fluorescence live cell imaging," Methods Cell Biol. **123**, 77–94 (2014).
15. C. Apelian, F. Harms, O. Thouvenin, *et al.*, "Dynamic full field optical coherence tomography: subcellular metabolic contrast revealed in tissues by interferometric signals temporal analysis," Biomed. Opt. Express **7**(4), 1511 (2016).
16. W. Tan, A. L. Oldenburg, J. J. Norman, *et al.*, "Optical coherence tomography of cell dynamics in three-dimensional tissue models," Opt. Express **14**(16), 7159 (2006).
17. L. Wang, M. Xu, L. Luo, *et al.*, "Iterative feedback bio-printing-derived cell-laden hydrogel scaffolds with optimal geometrical fidelity and cellular controllability," Sci. Rep. **8**(1), 2802 (2018).
18. C. J. Liu, J. T. Smith, Y. Wang, *et al.*, "Assessing cell viability with dynamic optical coherence microscopy," Biomed. Opt. Express **15**(3), 1408 (2024).
19. M. Münter, M. vom Endt, M. Pieper, *et al.*, "Dynamic contrast in scanning microscopic OCT," Opt. Lett. **45**(17), 4766 (2020).
20. S. Azzollini, T. Monfort, O. Thouvenin, *et al.*, "Dynamic optical coherence tomography for cell analysis [Invited]," Biomed. Opt. Express **14**(7), 3362 (2023).
21. O. Ronneberger, P. Fischer, and T. Brox, "U-Net: convolutional networks for biomedical image segmentation," arXiv (2015).
22. K. Simonyan and A. Zisserman, "Very deep convolutional networks for large-scale image recognition," arXiv (2014).
23. N. Siddique, S. Paheding, C. P. Elkin, *et al.*, "U-net and its variants for medical image segmesntation: a review of theory and applications," IEEE Access **9**, 82031–82057 (2021).
24. B. Wang, W. Wei, S. Qiu, *et al.*, "Boundary aware U-Net for retinal layers segmentation in optical coherence tomography images," IEEE J. Biomed. Health Inform. **25**(8), 3029–3040 (2021).
25. B. Belay, J. T. Koivisto, J. Parraga, *et al.*, "Optical projection tomography as a quantitative tool for analysis of cell morphology and density in 3D hydrogels," Sci. Rep. **11**(1), 6538 (2021).
26. A. Zein-Sabatto, A. Bico, M. Woo, *et al.*, "OCT Viability Imaging of 3D Microtissues," in *Optica Biophotonics Congress: Biomedical Optics 2024 (Translational, Microscopy, OCT, OTS, BRAIN)*, Optica Publishing Group, Fort Lauderdale, Florida, 2024, p. CS1E.4.
27. S. Tripathi, S. S. Mandal, and S. Bauri, "3D bioprinting and its innovative approach for biomedical applications," MedComm **4**(1), e194 (2023).

Biomedical Optics EXPRESS

28. A. Abaci, G. Camci-Unal, M. Guvendiren, *et al.*, "Three-dimensional bioprinting for medical applications," MRS Bull. **48**(6), 624–631 (2023).
29. M.-L. Yen, C.-C. Chien, I.-m. Chiu, *et al.*, "Multilineage differentiation and characterization of the human fetal osteoblastic 1.19 cell line: a possible in vitro model of human mesenchymal progenitors," Stem Cells Dayt. Ohio **25**(1), 125–131 (2007).
30. R. Armisen, "Agar and agarose biotechnological applications," Hydrobiologia **221**(1), 157–166 (1991).
31. Z. M. Jessop, N. Gao, S. Manivannan, *et al.*, "3D bioprinting cartilage," in *3D Bioprinting for Reconstructive Surgery*, Elsevier, 2018, pp. 277–304.
32. W. Drexler and J. G. Fujimoto, eds., "Optical Coherence Tomography: Technology and Applications," in *Biological and Medical Physics, Biomedical Engineering* (Springer Berlin Heidelberg, 2008.
33. X. Li, S. Cao, H. Liu, *et al.*, "Multi-Scale Reconstruction of Undersampled Spectral-Spatial OCT Data for Coronary Imaging Using Deep Learning," IEEE Trans. Biomed. Eng. **69**(12), 3667–3677 (2022).
34. S. Cao, X. Yao, N. Koirala, *et al.*, "Super-resolution technology to simultaneously improve optical & digital resolution of optical coherence tomography via deep learning," in *2020 42nd Annual International Conference of the IEEE Engineering in Medicine & Biology Society (EMBC)*, IEEE, Montreal, QC, Canada, Jul. 2020, 1879–1882.
35. A. J. Den Dekker and A. Van Den Bos, "Resolution: a survey," J. Opt. Soc. Am. A **14**(3), 547 (1997).
36. R. C. Gonzalez and R. E. Woods, *Digital image processing*, 4, Global edition. (Pearson Education, 2018).
37. I. Abd El-Sadek, A. Miyazawa, L. Tzu-Wei Shen, *et al.*, "Optical coherence tomography-based tissue dynamics imaging for longitudinal and drug response evaluation of tumor spheroids," Biomed. Opt. Express **11**(11), 6231 (2020).
38. H. M. Leung, M. L. Wang, H. Osman, *et al.*, "Imaging intracellular motion with dynamic micro-optical coherence tomography," Biomed. Opt. Express **11**(5), 2768–2778 (2020).
39. M. F. Khan, E. Khan, and Z. A. Abbasi, "Image contrast enhancement using normalized histogram equalization," Optik **126**(24), 4868–4875 (2015).
40. A. F. Agarap, "Deep Learning using Rectified Linear Units (ReLU)," arXiv (2018).
41. S. Ioffe and C. Szegedy, "Batch normalization: accelerating deep network training by reducing internal covariate shift," arXiv (2015).
42. H. Gholamalinezhad and H. Khosravi, "Pooling methods in deep neural networks, a review," arXiv (2020).
43. H. Abdi and L. J. Williams, "Principal component analysis," WIREs Comput. Stat. **2**(4), 433–459 (2010).
44. E. Madorran, A. Stožer, and Z. Arsov, "A Promising Method for the Determination of Cell Viability: The Membrane Potential Cell Viability Assay," Cells **11**(15), 2314 (2022).
45. H. Edelsbrunner and E. P. Mücke, "Three-dimensional alpha shapes," ACM Trans. Graph. **13**(1), 43–72 (1994).
46. M. Attene, "A lightweight approach to repairing digitized polygon meshes," Vis. Comput. **26**(11), 1393–1406 (2010).
47. B. Setzer, M. Bächle, M. C. Metzger, *et al.*, "The gene-expression and phenotypic response of hFOB 1.19 osteoblasts to surface-modified titanium and zirconia," Biomaterials **30**(6), 979–990 (2009).
48. H. J. Donahue, Z. Li, Z. Zhou, *et al.*, "Differentiation of human fetal osteoblastic cells and gap junctional intercellular communication," Am. J. Physiol.-Cell Physiol. **278**(2), C315–C322 (2000).
49. L. Liu, Z.-j. Fang, Y.-l. Zhang, *et al.*, "Decoding dynamic bamboo cell shrinkage with time-lapse microscopy and machine-learning," Ind. Crops Prod. **218**, 118965 (2024).
50. S. Kato, K. Suzuki, T. Kenjo, *et al.*, "Single-Cell Time-Lapse Observation Reveals Cell Shrinkage upon Cell Death in Batch Culture of Saccharomyces cerevisiae," mBio **12**(6), e03094 (2021).
51. A. B. Özdabak Sert, E. Bittrich, P. Uhlmann, *et al.*, "Monitoring Cell Adhesion on Polycaprolactone–Chitosan Films with Varying Blend Ratios by Quartz Crystal Microbalance with Dissipation," ACS Omega **8**(19), 17017–17027 (2023).
52. D. R. Green, "A Matter of Life and Death," Cold Spring Harb. Perspect. Biol. **14**(1), a041004 (2022).
53. Z. Li, C. Liu, B. Wang, *et al.*, "Heat treatment effect on the mechanical properties, roughness and bone ingrowth capacity of 3D printing porous titanium alloy," RSC Adv. **8**(22), 12471–12483 (2018).
54. C.-W. Chen, M. W. Betz, J. P. Fisher, *et al.*, "Macroporous hydrogel scaffolds and their characterization by optical coherence tomography," Tissue Eng. Part C Methods **17**(1), 101–112 (2011).
55. S.-P. Yang and T.-M. Lee, "The effect of substrate topography on hFOB cell behavior and initial cell adhesion evaluated by a cytodetacher," J. Mater. Sci. Mater. Med. **22**(4), 1027–1036 (2011).
56. C. J. Gomes, M. W. Harman, S. M. Centuori, *et al.*, "Measuring DNA content in live cells by fluorescence microscopy," Cell Div. **13**(1), 6 (2018).
57. Y. Al-Kofahi, W. Lassoued, W. Lee, *et al.*, "Improved Automatic Detection and Segmentation of Cell Nuclei in Histopathology Images," IEEE Trans. Biomed. Eng. **57**(4), 841–852 (2010).
58. L. Wang, M. Xu, L. Zhang, *et al.*, "Automated quantitative assessment of three-dimensional bioprinted hydrogel scaffolds using optical coherence tomography," Biomed. Opt. Express **7**(3), 894 (2016).